

Production of Charged Pions and Hadrons in Au+Au Collisions at $\sqrt{s_{NN}} = 130$ GeV

J. Adams,³ C. Adler,¹² M.M. Aggarwal,²⁵ Z. Ahammed,³⁸ J. Amonett,¹⁷ B.D. Anderson,¹⁷ M. Anderson,⁵ D. Arkhipkin,¹¹ G.S. Averichev,¹⁰ S.K. Badyal,¹⁶ J. Balewski,¹³ O. Barannikova,^{28,10} L.S. Barnby,³ J. Baudot,¹⁵ S. Bekele,²⁴ V.V. Belaga,¹⁰ R. Bellwied,⁴¹ J. Berger,¹² B.I. Bezverkhny,⁴³ S. Bhardwaj,²⁹ P. Bhaskar,³⁸ A.K. Bhati,²⁵ H. Bichsel,⁴⁰ A. Billmeier,⁴¹ L.C. Bland,² C.O. Blyth,³ B.E. Bonner,³⁰ M. Botje,²³ A. Boucham,³⁴ A. Brandin,²¹ A. Bravar,² R.V. Cadman,¹ X.Z. Cai,³³ H. Caines,⁴³ M. Calderón de la Barca Sánchez,² J. Carroll,¹⁸ J. Castillo,¹⁸ M. Castro,⁴¹ D. Cebra,⁵ P. Chaloupka,⁹ S. Chattopadhyay,³⁸ H.F. Chen,³² Y. Chen,⁶ S.P. Chernenko,¹⁰ M. Cherney,⁸ A. Chikanian,⁴³ B. Choi,³⁶ W. Christie,² J.P. Coffin,¹⁵ T.M. Cormier,⁴¹ J.G. Cramer,⁴⁰ H.J. Crawford,⁴ D. Das,³⁸ S. Das,³⁸ A.A. Derevschikov,²⁷ L. Didenko,² T. Dietel,¹² W.J. Dong,⁶ X. Dong,^{32,18} J.E. Draper,⁵ F. Du,⁴³ A.K. Dubey,¹⁴ V.B. Dunin,¹⁰ J.C. Dunlop,² M.R. Dutta Majumdar,³⁸ V. Eckardt,¹⁹ L.G. Efimov,¹⁰ V. Emelianov,²¹ J. Engelage,⁴ G. Eppley,³⁰ B. Erasmus,³⁴ M. Estienne,³⁴ P. Fachini,² V. Faine,² J. Faivre,¹⁵ R. Fatemi,¹³ K. Filimonov,¹⁸ P. Filip,⁹ E. Finch,⁴³ Y. Fisyak,² D. Flierl,¹² K.J. Foley,² J. Fu,⁴² C.A. Gagliardi,³⁵ N. Gagunashvili,¹⁰ J. Gans,⁴³ M.S. Ganti,³⁸ L. Gaudichet,³⁴ M. Germain,¹⁵ F. Geurts,³⁰ V. Ghazikhanian,⁶ P. Ghosh,³⁸ J.E. Gonzalez,⁶ O. Grachov,⁴¹ V. Grigoriev,²¹ S. Gronstal,⁸ D. Grosnick,³⁷ M. Guedon,¹⁵ S.M. Guertin,⁶ A. Gupta,¹⁶ E. Gushin,²¹ T.D. Gutierrez,⁵ T.J. Hallman,² D. Hardtke,¹⁸ J.W. Harris,⁴³ M. Heinz,⁴³ T.W. Henry,³⁵ S. Heppelmann,²⁶ T. Herston,²⁸ B. Hippolyte,⁴³ A. Hirsch,²⁸ E. Hjort,¹⁸ G.W. Hoffmann,³⁶ M. Horsley,⁴³ H.Z. Huang,⁶ S.L. Huang,³² T.J. Humanic,²⁴ G. Igo,⁶ A. Ishihara,³⁶ P. Jacobs,¹⁸ W.W. Jacobs,¹³ M. Janik,³⁹ H. Jiang,^{6,18} I. Johnson,¹⁸ P.G. Jones,³ E.G. Judd,⁴ S. Kabana,⁴³ M. Kaneta,¹⁸ M. Kaplan,⁷ D. Keane,¹⁷ V.Yu. Khodyrev,²⁷ J. Kirelyuk,⁶ A. Kisiel,³⁹ J. Klay,¹⁸ S.R. Klein,¹⁸ A. Klyachko,¹³ D.D. Koetke,³⁷ T. Kollegger,¹² M. Kopytine,¹⁷ L. Kotchenda,²¹ A.D. Kovalenko,¹⁰ M. Kramer,²² P. Kravtsov,²¹ V.I. Kravtsov,²⁷ K. Krueger,¹ C. Kuhn,¹⁵ A.I. Kulikov,¹⁰ A. Kumar,²⁵ G.J. Kunde,⁴³ C.L. Kunz,⁷ R.Kh. Kutuev,¹¹ A.A. Kuznetsov,¹⁰ M.A.C. Lamont,³ J.M. Landgraf,² S. Lange,¹² C.P. Lansdell,³⁶ B. Lasiuk,⁴³ F. Laue,² J. Lauret,² A. Lebedev,² R. Lednický,¹⁰ M.J. LeVine,² C. Li,³² Q. Li,⁴¹ S.J. Lindenbaum,²² M.A. Lisa,²⁴ F. Liu,⁴² L. Liu,⁴² Z. Liu,⁴² Q.J. Liu,⁴⁰ T. Ljubicic,² W.J. Llope,³⁰ H. Long,⁶ R.S. Longacre,² M. Lopez-Noriega,²⁴ W.A. Love,² T. Ludlam,² D. Lynn,² J. Ma,⁶ Y.G. Ma,³³ D. Magestro,²⁴ S. Mahajan,¹⁶ L.K. Mangotra,¹⁶ D.P. Mahapatra,¹⁴ R. Majka,⁴³ R. Manweiler,³⁷ S. Margetis,¹⁷ C. Markert,⁴³ L. Martin,³⁴ J. Marx,¹⁸ H.S. Matis,¹⁸ Yu.A. Matulenko,²⁷ T.S. McShane,⁸ F. Meissner,¹⁸ Yu. Melnick,²⁷ A. Meschanin,²⁷ M. Messer,² M.L. Miller,⁴³ Z. Milosevich,⁷ N.G. Minaev,²⁷ C. Mironov,¹⁷ D. Mishra,¹⁴ J. Mitchell,³⁰ B. Mohanty,³⁸ L. Molnar,²⁸ C.F. Moore,³⁶ M.J. Mora-Corral,¹⁹ D.A. Morozov,²⁷ V. Morozov,¹⁸ M.M. de Moura,³¹ M.G. Munhoz,³¹ B.K. Nandi,³⁸ S.K. Nayak,¹⁶ T.K. Nayak,³⁸ J.M. Nelson,³ P. Nevski,² V.A. Nikitin,¹¹ L.V. Nogach,²⁷ B. Norman,¹⁷ S.B. Nurushev,²⁷ G. Odyniec,¹⁸ A. Ogawa,² V. Okorokov,²¹ M. Oldenburg,¹⁸ D. Olson,¹⁸ G. Paic,²⁴ S.U. Pandey,⁴¹ S.K. Pal,³⁸ Y. Panebratsev,¹⁰ S.Y. Panitkin,² A.I. Pavlinov,⁴¹ T. Pawlak,³⁹ V. Perevoztchikov,² C. Perkins,⁴ W. Peryt,³⁹ V.A. Petrov,¹¹ S.C. Phatak,¹⁴ R. Picha,⁵ M. Planinic,⁴⁴ J. Pluta,³⁹ N. Porile,²⁸ J. Porter,² A.M. Poskanzer,¹⁸ M. Potekhin,² E. Potrebenikova,¹⁰ B.V.K.S. Potukuchi,¹⁶ D. Prindle,⁴⁰ C. Pruneau,⁴¹ J. Putschke,¹⁹ G. Rai,¹⁸ G. Rakness,¹³ R. Raniwala,²⁹ S. Raniwala,²⁹ O. Ravel,³⁴ R.L. Ray,³⁶ S.V. Razin,^{10,13} D. Reichhold,²⁸ J.G. Reid,⁴⁰ G. Renault,³⁴ F. Retiere,¹⁸ A. Ridiger,²¹ H.G. Ritter,¹⁸ J.B. Roberts,³⁰ O.V. Rogachevski,¹⁰ J.L. Romero,⁵ A. Rose,⁴¹ C. Roy,³⁴ L.J. Ruan,^{32,2} R. Sahoo,¹⁴ I. Sakrejda,¹⁸ S. Salur,⁴³ J. Sandweiss,⁴³ I. Savin,¹¹ J. Schambach,³⁶ R.P. Scharenberg,²⁸ N. Schmitz,¹⁹ L.S. Schroeder,¹⁸ K. Schweda,¹⁸ J. Seger,⁸ D. Seliverstov,²¹ P. Seyboth,¹⁹ E. Shahaliev,¹⁰ M. Shao,³² M. Sharma,²⁵ K.E. Shestermanov,²⁷ S.S. Shimanskii,¹⁰ R.N. Singaraju,³⁸ F. Simon,¹⁹ G. Skoro,¹⁰ N. Smirnov,⁴³ R. Snellings,²³ G. Sood,²⁵ P. Sorensen,¹⁸ J. Sowinski,¹³ H.M. Spinka,¹ B. Srivastava,²⁸ S. Stanislaus,³⁷ R. Stock,¹² A. Stolpovsky,⁴¹ M. Strikhanov,²¹ B. Stringfellow,²⁸ C. Struck,¹² A.A.P. Suaide,³¹ E. Sugarbaker,²⁴ C. Suire,² M. Šumbera,⁹ B. Surrow,² T.J.M. Symons,¹⁸ A. Szanto de Toledo,³¹ P. Szarwas,³⁹ A. Tai,⁶ J. Takahashi,³¹ A.H. Tang,^{2,23} D. Thein,⁶ J.H. Thomas,¹⁸ V. Tikhomirov,²¹ M. Tokarev,¹⁰ M.B. Tonjes,²⁰ T.A. Trainor,⁴⁰ S. Trentalange,⁶ R.E. Tribble,³⁵ M.D. Trivedi,³⁸ V. Trofimov,²¹ O. Tsai,⁶ T. Ullrich,² D.G. Underwood,¹ G. Van Buren,² A.M. VanderMolen,²⁰ A.N. Vasiliev,²⁷ M. Vasiliev,³⁵ S.E. Vigdor,¹³ Y.P. Viyogi,³⁸ S.A. Voloshin,⁴¹ W. Waggoner,⁸ F. Wang,²⁸ G. Wang,¹⁷ X.L. Wang,³² Z.M. Wang,³² H. Ward,³⁶ J.W. Watson,¹⁷ R. Wells,²⁴ G.D. Westfall,²⁰ C. Whitten Jr.,⁶ H. Wieman,¹⁸ R. Willson,²⁴ S.W. Wissink,¹³ R. Witt,⁴³ J. Wood,⁶ J. Wu,³² N. Xu,¹⁸ Z. Xu,² Z.Z. Xu,³² E. Yamamoto,¹⁸ P. Yepes,³⁰ V.I. Yurevich,¹⁰ Y.V. Zanevski,¹⁰ I. Zborovský,⁹ H. Zhang,^{43,2} W.M. Zhang,¹⁷ Z.P. Zhang,³² P.A. Żolnierczuk,¹³ R. Zoulkarneev,¹¹ J. Zoulkarneeva,¹¹ and A.N. Zubarev¹⁰

(STAR Collaboration)*

¹Argonne National Laboratory, Argonne, Illinois 60439

- ²Brookhaven National Laboratory, Upton, New York 11973
³University of Birmingham, Birmingham, United Kingdom
⁴University of California, Berkeley, California 94720
⁵University of California, Davis, California 95616
⁶University of California, Los Angeles, California 90095
⁷Carnegie Mellon University, Pittsburgh, Pennsylvania 15213
⁸Creighton University, Omaha, Nebraska 68178
⁹Nuclear Physics Institute AS CR, Řež/Prague, Czech Republic
¹⁰Laboratory for High Energy (JINR), Dubna, Russia
¹¹Particle Physics Laboratory (JINR), Dubna, Russia
¹²University of Frankfurt, Frankfurt, Germany
¹³Indiana University, Bloomington, Indiana 47408
¹⁴Institute of Physics, Bhubaneswar 751005, India
¹⁵Institut de Recherches Subatomiques, Strasbourg, France
¹⁶University of Jammu, Jammu 180001, India
¹⁷Kent State University, Kent, Ohio 44242
¹⁸Lawrence Berkeley National Laboratory, Berkeley, California 94720
¹⁹Max-Planck-Institut für Physik, Munich, Germany
²⁰Michigan State University, East Lansing, Michigan 48824
²¹Moscow Engineering Physics Institute, Moscow Russia
²²City College of New York, New York City, New York 10031
²³NIKHEF, Amsterdam, The Netherlands
²⁴Ohio State University, Columbus, Ohio 43210
²⁵Panjab University, Chandigarh 160014, India
²⁶Pennsylvania State University, University Park, Pennsylvania 16802
²⁷Institute of High Energy Physics, Protvino, Russia
²⁸Purdue University, West Lafayette, Indiana 47907
²⁹University of Rajasthan, Jaipur 302004, India
³⁰Rice University, Houston, Texas 77251
³¹Universidade de Sao Paulo, Sao Paulo, Brazil
³²University of Science & Technology of China, Anhui 230027, China
³³Shanghai Institute of Nuclear Research, Shanghai 201800, P.R. China
³⁴SUBATECH, Nantes, France
³⁵Texas A&M, College Station, Texas 77843
³⁶University of Texas, Austin, Texas 78712
³⁷Valparaiso University, Valparaiso, Indiana 46383
³⁸Variable Energy Cyclotron Centre, Kolkata 700064, India
³⁹Warsaw University of Technology, Warsaw, Poland
⁴⁰University of Washington, Seattle, Washington 98195
⁴¹Wayne State University, Detroit, Michigan 48201
⁴²Institute of Particle Physics, CCNU (HZNU), Wuhan, 430079 China
⁴³Yale University, New Haven, Connecticut 06520
⁴⁴University of Zagreb, Zagreb, HR-10002, Croatia
- (Dated: August 8, 2019)

The STAR experiment has measured the production of charged hadrons and identified charged pions as a function of transverse momentum, (pseudo-)rapidity, and centrality in Au+Au collisions at $\sqrt{s_{NN}} = 130$ GeV. The mean transverse momentum of charged hadrons (pions) increases by roughly 22%(15%) from peripheral to central collisions. As a function of (pseudo-)rapidity, the measured yields and spectral shapes are consistent with a Lorentz-boost invariant mid-rapidity region at least within $|y| < 0.5$ for all collision centralities. We compare our measurements of the integrated charged particle (pseudo-)rapidity density per participating nucleon-pair with two models representing different phenomenological concepts of particle production and featuring opposing parameterizations of the centrality dependence of the rapidity density. We furthermore explore the discriminating power of our measurement against the theoretical calculations in the light of uncertainties originating from the determination of the average number of participating nucleons $\langle N_{part} \rangle$.

I. INTRODUCTION

*URL: www.star.bnl.gov

High-energy heavy-ion collisions as provided by the Relativistic Heavy Ion Collider (RHIC) are expected to

yield energy densities sufficiently high to create a new state of nuclear matter, a plasma of quasi-free quarks and gluons. In its evolution, this new state would undergo a phase transition to form a fireball of normal nuclear matter confined in hadrons, which would further be subject to a rapid expansion. The dominant fraction of the hadrons produced in heavy ion collisions originates from this hadronic stage. Nevertheless, global observables such as rapidity and transverse energy densities of hadrons are believed to provide an important constraint to the initial conditions and have been studied [1, 2, 3, 4, 5, 6].

In this report, we provide a brief description of the STAR experiment and a detailed description of the analysis of the Au+Au collision data at $\sqrt{s_{NN}} = 130$ GeV in sections II and III, respectively. In chapter IV we present transverse momentum distributions of charged hadrons (h^\pm) and pions (π^\pm) in the mid-rapidity region. Characterizing them by their mean transverse momenta $\langle p_T \rangle$ and integrated yields $dN/d\eta$, we study their centrality dependence. Here, we especially focus on the normalized charged hadron pseudo-rapidity density ($2/N_{part}$) ($dN_{ch}/d\eta$), since it has been argued that this key observable might distinguish between different theoretical estimates of the initial conditions [7]. We discuss the limitations placed on the discriminating power of this measurement due to uncertainties on the determination of the average number of participant nucleons $\langle N_{part} \rangle$ in a given centrality bin.

We will furthermore study the (pseudo-)rapidity dependence of charged hadron and pion production in order to investigate whether the assumption of a Lorentz-boost invariant source holds. This assumption is critical for many theoretical calculations such as the Bjorken (transverse) energy density [8] which we will calculate as a function of centrality.

II. EXPERIMENTAL SETUP

The data presented in this paper were taken with the STAR detector [9, 10] during the first run of Brookhaven National Laboratory's RHIC collider in 2000 (Run I).

The main components of STAR were a solenoidal magnet, a large acceptance Time Projection Chamber (TPC) as the primary tracking device for charged particles, a small acceptance Ring Imaging Cherenkov (RICH) detector for high momentum particle identification (not used in this analysis), as well as two Zero Degree Calorimeters (ZDC) and a Central Trigger Barrel (CTB) for triggering purposes.

The magnet is able to provide a homogeneous magnetic flux density of up to $|B_z| = 0.5$ Tesla (operated at ± 0.25 Tesla for the data presented here) parallel to the beam (z) axis and houses the TPC, the RICH, and the CTB. The trajectories of charged hadrons inside the TPC can be described as helices. Small inhomogeneities on the order of $5 \cdot 10^{-4}$ Tesla can easily be identified and

corrected for when studying the decay of neutral particles, e.g. K_s^0 , into charged particles.

For a charged particle ideally originating from the center of the TPC at $x = y = z = 0$ cm the TPC has full azimuthal coverage, while coverage in pseudo-rapidity is limited to $|\eta| < 2.1$. However, requiring that the particle exits the active volume through the outer field cage, leaving signals on all 45 pad-rows, would restrict the pseudo-rapidity coverage to $|\eta| < 0.9$.

The two ZDCs [11] are located on the beam axis at ± 18 m distance from the TPC center, covering emission angles of $\theta < 4$ mrad. They measure neutrons at beam rapidity originating from the break up of the colliding nuclei, while charged fragments get swept away by the same beam steering magnets that bend the incoming nuclei towards the interaction point. During data taking, coincident signals in the ZDCs were the only trigger requirement when recording the minimum bias event sample. The number of neutrons detected in the ZDCs can be identified with the amount of energy deposited.

The CTB consists of 240 scintillator slats arranged around the outer diameter of the TPC. With full azimuthal coverage over $|\eta| < 1$ and an efficiency $\epsilon_{CTB} \approx 1$ for minimum ionizing particles, it provides a good estimate of the number of charged particles produced in the mid-rapidity region.

Correlating the energy deposition in the ZDCs with the number of minimum ionizing particles detected by the CTB as shown in Fig. 1 (the energy on both the ZDC and the CTB axis is given in units of analog to digital converter(ADC) channels) can be used to determine the collision centrality. During data taking a central event trigger (selecting the approximately 15% most central events) was implemented by requiring coincident signals between the two ZDCs and the CTB signal exceeding a predetermined threshold. For more details please refer to Ref. [12].

During Run I, STAR recorded about $2 \cdot 10^6$ Au+Au collisions at $\sqrt{s_{NN}} = 130$ GeV, roughly equally divided between the minimum bias and central event triggers [1].

III. ANALYSIS

A. Reconstruction

After the TPC raw data have been calibrated, the reconstruction of events consists of the following four steps: cluster finding, global track-finding and fitting, primary vertex fitting, and primary track re-fitting.

First, a cluster finder gathers the TPC data into clusters in 2D space and time direction. They are subsequently converted into 3D space-points in the global STAR coordinate system, where drift velocity and trigger-time offset are taken into account. Their integrated and gain calibrated charge is used for particle identification via the dE/dx measurement (see IIID). For

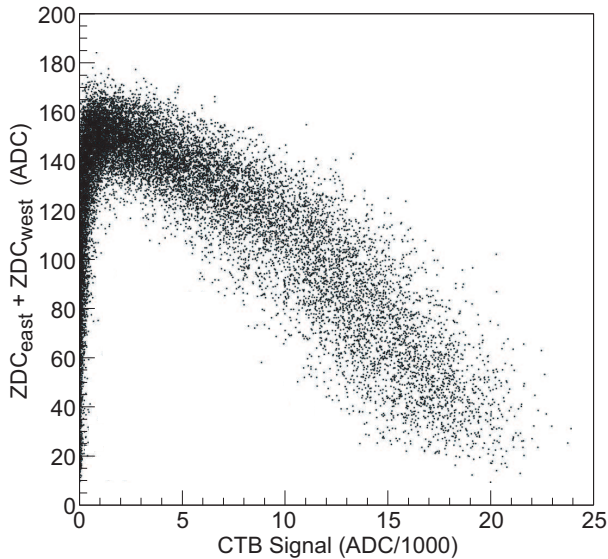


FIG. 1: ZDC signal (sum of west and east ZDCs) vs the CTB signal. Centrality of the collision increases as one progresses first upward along the left edge, then from left to right along the observed locus.

more detail on the calibration and cluster finding in the TPC, see Ref. [13].

Operating on these space-points, a *follow-your-nose* tracker works its way from the outer pad-rows inwards, gathering space-points into tracks. These tracks are then passed through a Kalman filter [14, 15], calculating the track parameters while taking energy loss and multiple scattering in the beam pipe and detector material into account. These *global* tracks are then extrapolated towards the beam-axis in the center of the TPC and a common origin is sought, which can be identified as the primary vertex.

Once the primary vertex is found, all global tracks which point back to the newly found primary vertex within 3 cm or less, undergo a second pass through the Kalman filter, this time taking the primary vertex into account. We label these tracks as *primary* tracks. From simulations, we determine the momentum resolutions for primary tracks to be $\delta p/p = [0.016 (p_T/(\text{GeV}/c)) + 0.012]^{-1}$ for central events and $\delta p/p = [0.011 (p_T/(\text{GeV}/c)) + 0.013]^{-1}$ for peripheral events.

B. Event Selection and Efficiency

The data presented in this paper were analysed using only the TPC as the main tracking device as well as the CTB and the two ZDCs for triggering purposes. Out of the minimum bias event sample taken by STAR during RHIC Run I, we selected about 200k events by requiring the reconstructed primary vertex to be within ± 30 cm of the center of the TPC along the beam axis. This selection

ensures that particles within a pseudo-rapidity window of $|\eta| < 1$ lie well within the acceptance of the TPC.

As depicted in Fig. 1, the ZDC does not allow an unambiguous selection of events into centrality classes due to a sharp turnover for peripheral collisions at CTB (ADC) ≈ 1500 . In order to establish different centrality bins, we divided our data sample into 10 multiplicity classes. Here, multiplicity is defined as the number of charged tracks within the pseudo-rapidity interval $|\eta| < 0.5$ and a transverse momentum $p_T > 0.1$ GeV/c. The reason for this particular phase-space interval is its high and almost constant acceptance and efficiency $\epsilon_{acc} \cdot \epsilon_{eff} \approx 0.8$. First, the multiplicity distribution dN/dN_{ch} was recorded and corrected for trigger and vertex-finding inefficiencies at very low number of charged particles $N_{ch} < 50$. This was done by scaling the uncorrected distribution to the same integral as a corresponding distribution obtained from the Hijing model [16, 17] in the range $50 < N_{ch} < 100$. Here the collision dynamics is dominated by "geometry", which is well described by the Hijing model as shown in earlier publications [1]. The trigger efficiency $\epsilon_{trig}(N_{ch})$ was evaluated as the ratio of the recorded and the Hijing dN/dN_{ch} distributions. The trigger efficiency corrected multiplicity distribution dN_{trig}/dN_{ch} was calculated by weighting events according to $\epsilon_{trig}(N_{ch})$ for $N_{ch} < 50$. Following this procedure the overall trigger efficiency evaluates to $94 \pm 3\%$, but is only about 60% for very peripheral events with less than 5 tracks [1, 18].

At this point, the efficiency corrected multiplicity distribution dN_{trig}/dN_{ch} does not yet represent the physics distribution dN/dN_{ch} describing the collisions, since no track efficiency and acceptance corrections were applied when counting the charged particles. However, it is already possible to define multiplicity classes in terms of fractions of the total inelastic hadronic cross-section in N_{ch} (see Fig. 2 and Table I).

class #	$\sigma/\sigma_{tot}(\%)$	$N_{ch} (p_T > 0.1 \text{ GeV}/c, \eta < 0.5)$
10	0-5	>424
9	5-10	357-424
8	10-20	255-357
7	20-30	175-255
6	30-40	115-175
5	40-50	71-115
4	50-60	41-71
3	60-70	20-41
2	70-80	9-20
1	80-100	0-9

TABLE I: Definition of the multiplicity classes via the uncorrected charged track multiplicity in the reference window $|\eta| < 0.5$ and $p_T > 0.1$ GeV/c.

In the fully corrected $d\sigma/dN_{ch}$ distribution the boundaries between the multiplicity classes are slightly smeared out due to the fact that the track-by-track corrections depend on five partially correlated parameters: momentum, pseudo-rapidity, particle type, event multiplicity,

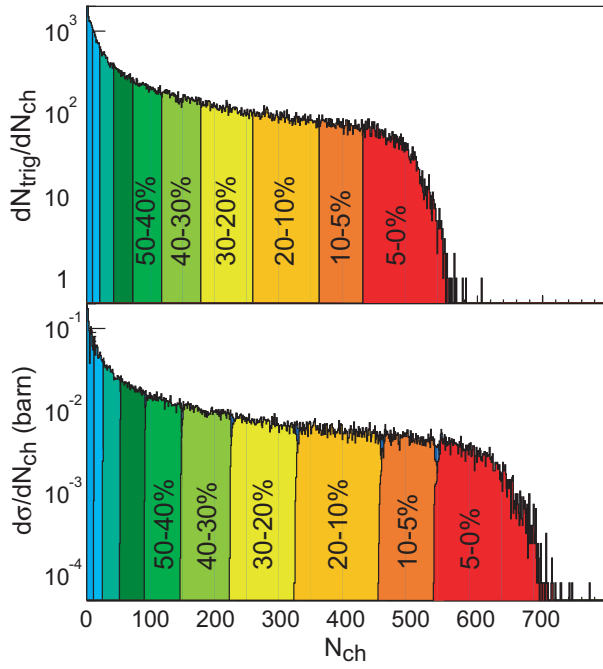


FIG. 2: Top: Definition of the centrality by dividing the uncorrected dN/dN_{ch} distributions into multiplicity classes. Bottom: The fully corrected and normalized $d\sigma/dN_{ch}$ distribution.

and event primary vertex z-position. With an assumed hadronic cross-section of 6.9 b for Au+Au collisions at $\sqrt{s_{NN}} = 130$ GeV given by the Hijing model, the corrected distribution can now be normalized and be written as $d\sigma/dN_{ch}$ as shown in the lower panel of Fig. 2.

Estimating the background contribution (e.g., from beam-gas and photon-nuclear interaction) to the 100-80% centrality bin to be about 30%, we exclude this bin from further analysis. All the results presented in section IV reflect the remaining 9 bins only.

We acknowledge that it is possible to first construct the fully corrected dN/dN_{ch} in an iterative process and then divide it into multiplicity classes, but refrain from doing so for purely practical reasons. We verified that for all of our multiplicity classes the mean number of charged particles $\langle dN/dN_{ch} \rangle$ agrees within 2% regardless whether we first fully correct and then slice into multiplicity classes or vice versa.

C. Track Efficiencies and Corrections

In order to record the corrected dN/dN_{ch} , or any other charged particle distribution, we apply various corrections on a track-by-track basis. They are:

1. geometrical acceptance
2. decay losses (e.g. $\pi, K \rightarrow \mu\nu$)
3. efficiency

4. energy loss in the detector material
5. track merging and splitting
6. ghost tracks
7. weak decay feed-down (e.g. $K_s^0 \rightarrow \pi\pi$; $\Lambda \rightarrow N\pi$)
8. particle misidentification (e.g. leptons misidentified as hadrons)
9. secondary interaction background (mainly antiproton annihilation in the detector material: $\bar{p} N \rightarrow \pi X$ and proton knock-out in the beam pipe: $\pi Be \rightarrow p\pi X$)

To calculate these corrections we make use of the embedding technique, where simulated tracks are blended into real events.

For a representative sample of our recorded raw data, we first run our regular reconstruction software to obtain the primary vertex position and the track multiplicity.

In the following step, fed by interchangeable event generators [51], a so-called *Monte Carlo* event with the same primary vertex position is created. This is done using the GEANT program which propagates particles originating from the event generators through a detailed detector model. The traces of charged particles in the TPC are simulated starting with the initial ionization of the TPC gas, then the electron transport and multiplication in the drift field, and finally the induced signal on the TPC's read-out pads and the response of read-out electronics. The resulting artificial events are of the same format and contain the same information as real raw data events delivered by the data acquisition system. In the next step, these events are embedded into the real events by adding their raw data information. Detector effects such as the saturation of ADC channels are taken into account. These mixed raw data events are then processed by the standard reconstruction software which translates the raw detector information into space points in the TPC volume and ultimately gathers them together into (*reconstructed*) tracks. In the final step, an association between Monte Carlo and reconstructed tracks is created by matching tracks occupying the same coordinate space.

Having the initial event generator information, the Monte Carlo and the reconstructed tracks, as well as the track associations at hand, detector acceptances and efficiencies can now be evaluated. The former are calculated as the fraction of initially generated particles resulting in Monte Carlo tracks and are shown in Fig. 3a as a function of transverse momentum in the rapidity window $|y| < 1$ for primary π^- , K^- , and \bar{p} . The acceptance for pions is mainly determined by the detector geometry and geometric track quality requirements such as the length in the active TPC volume and the minimum number of hits per track. Similar to pions, the p and \bar{p} acceptance is dominated by detector geometry for momenta $p_T > 1$ GeV/c. However, for lower momenta the larger energy loss and absorption in the detector and beam pipe material become important and lead to a reduced acceptance. For

K^\pm , the acceptance is a convolution of the geometrical acceptance and the losses due to the short decay length

of the K -meson ($c\tau \approx 3.7$ m). As Fig. 3a demonstrates, the latter is clearly dominating for $p_T < 1$ GeV/c.

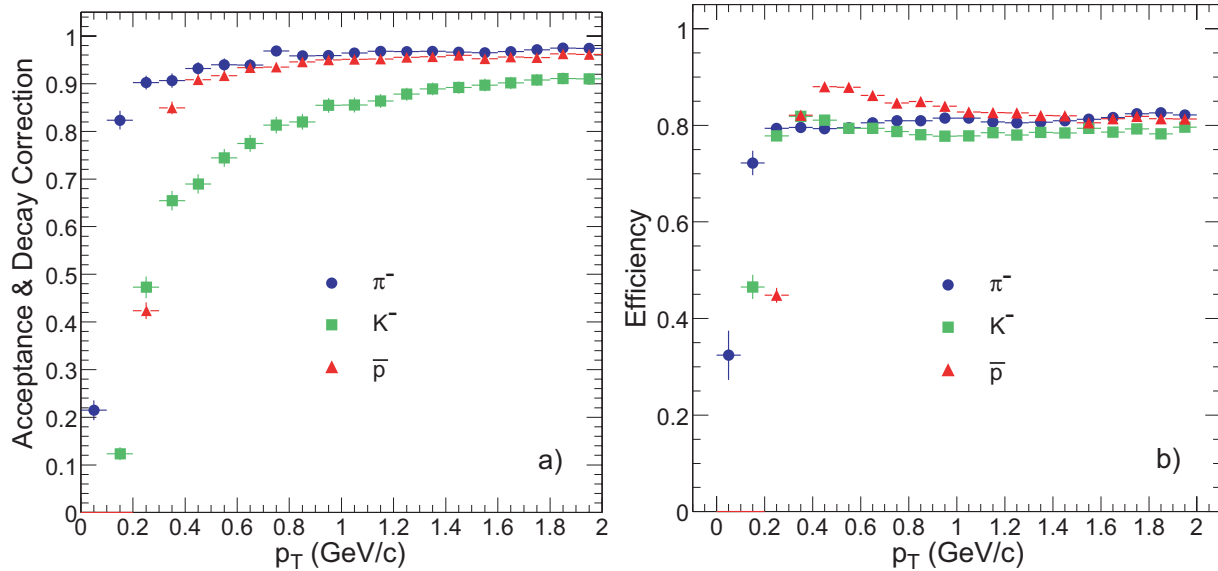


FIG. 3: Acceptance due to detector geometry and decay losses (left) and reconstruction efficiency (right) for primary π^- , K^- , and \bar{p} in the rapidity interval $|y| < 1$.

The efficiency of the track reconstruction is defined as the fraction of the embedded Monte Carlo tracks that can be associated to reconstructed tracks. Here, we limit the number of embedded tracks to 5% of the real event's multiplicity. Pure simulations without embedding into real events yield approximately 5% higher efficiencies than those obtained using the embedding technique. We attribute this difference to background from non primary particles and electronic noise in the TPC that can not be properly represented in simulations. Figure 3b shows the reconstruction efficiencies as a function of the transverse momentum as evaluated by the embedding process for π^- , K^- , and \bar{p} in the phase-space region $0.1 < p_T/(\text{GeV}/c) < 2.0$ and $|\eta| < 1$.

After acceptance and efficiency corrections are applied we further correct for split, merged, and ghost tracks [52] as well as for tracks originating from secondary interactions (i.e. proton knock-out in the beam pipe). Together they constitute less than 1% of the total yield.

Finally, we correct the spectra for feed-down from K^0 , Λ and $\bar{\Lambda}$ decays, the most dominant sources of weak decay background using the invariant cross sections measured by STAR [19]. Depending on the track quality requirements, the contribution of non-primary tracks can be as high as 25% for $p_T < 0.2$ GeV/c particles, but is only $\approx 8\%$ on average.

All the corrections described above not only depend on particle type and transverse momentum, but also on rapidity, on the event multiplicity, on the primary vertex position, and on the track quality criteria and have been evaluated as such. However, their functional dependence on p_T is dominating and Figs. 3a and 3b show acceptance and efficiency corrections for the approximately 5% most central events for $|y| < 1$ and primary vertex positions $|z| < 30$ cm.

D. Particle Identification

For the pion data presented in this manuscript, we correlate the charged particles' specific ionization dE/dx with their rigidity (momentum / charge) for particle identification (depicted in Fig. 4). However, since the resolution ($\approx 8\%$) of our ionization measurement prohibits unambiguous pion identification, we use a statistical method to determine the pion yields. We form the quantity

$$Z = \frac{\ln(I_{meas}/I_{exp}(\mathbf{p}, m))}{\sigma_{dE/dx}}, \quad (1)$$

where I_{meas} and I_{exp} are the measured and expected ionization in the TPC for a particle of momentum p

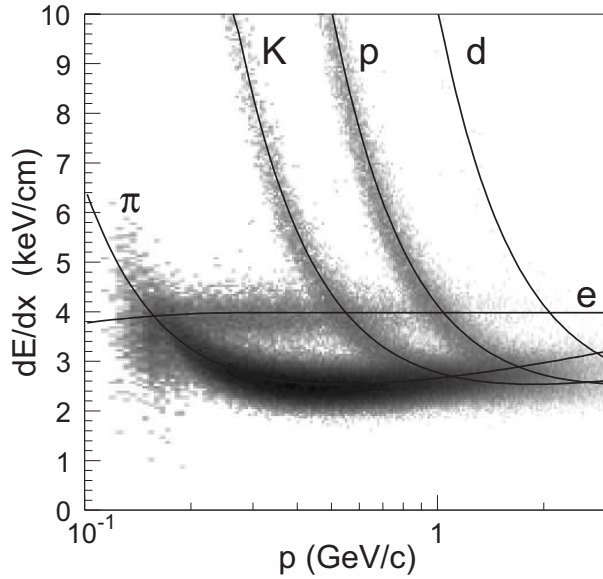


FIG. 4: Correlation of charged particle specific ionization dE/dx with momentum (assuming the charge $q = 1$). The lines present the expectations for e^\pm , π^\pm , K^\pm , p , \bar{p} , and d according to the Bethe-Bloch formula.

and mass m , and $\sigma_{dE/dx}$ is the resolution of the specific ionization in the TPC gas. The Z distribution for a given momentum p can be described as a superposition of Gaussians, one per particle species. For $Z_\pi = Z|_{m=m_\pi}$, the Gaussians representing the pions have the same widths and means for all momenta (Fig. 5). The

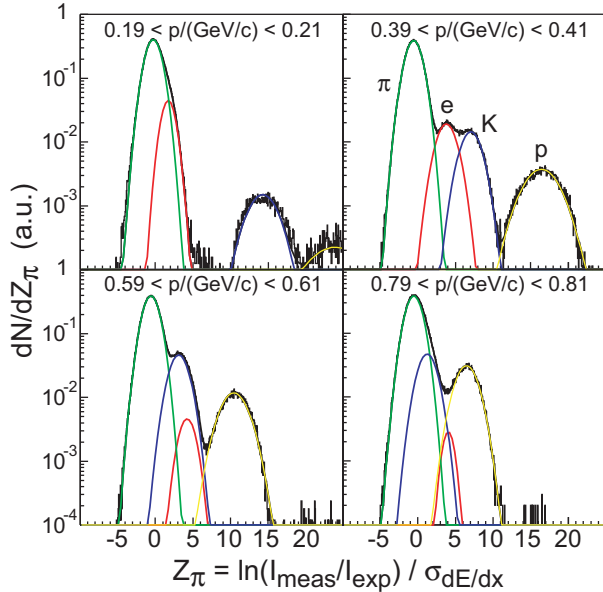


FIG. 5: Statistical identification of pions using the Z_π variable for several p_T intervals and $0.2 < y < 0.3$.

means of all other Gaussians and their widths are momentum dependent. For a particle of a given momentum p and I_{meas} , we evaluate the probability of being a

pion from the relative yield of the corresponding Gaussian compared to the Z distribution. This method breaks down at about $p = 0.8$ GeV/c where the dE/dx bands completely overlap and the fitting of the pion Gaussian becomes unreliable.

IV. RESULTS

A. Charged Hadrons

After applying the corrections described in Section III, we calculate the double differential distributions $(1/p_T) d^2N/(dp_T d\eta)$ as a function of the transverse momentum p_T for positively and negatively charged hadrons in 9 centrality and 20 rapidity intervals. Figures 6 and 7 show the centrality dependence of the mid-rapidity region $|\eta| < 0.5$, and the pseudo-rapidity dependence for our most central (top 5%) data sample, respectively.

In all four panels, we scale the distributions by successive powers of 2 for clarity. The uncorrelated statistical uncertainties are smaller than the symbols for most of the data points. Not shown are the correlated systematic uncertainties of about 7% originating from uncertainties on the corrections applied to the raw data as described in section III. They have been estimated by varying track quality requirements and by comparing distributions measuring the same regions of phase-space in different regions of the TPC. A power-law function of the form

$$\frac{1}{p_T} \frac{d^2N}{dp_T d\eta} = C \left(1 + \frac{2p_T}{\langle p_T \rangle (n-3)} \right)^{-n} \quad (2)$$

is fit to the data (lines). The fits describe the data well over the whole range. Assuming the power-law shape, we measure about 80% of the estimated yield within the fit range $0.2 < p_T/(\text{GeV}/c) < 2.0$. The charged hadron yields quoted in Ref. [18] are about 2.5% lower due to the use of an extended fit range in order to parameterize the shape of the p_T -spectra up to $p_T = 6$ GeV/c. In Fig. 8, the $\langle p_T \rangle$ parameters are shown as a function of the number of participants $\langle N_{part} \rangle$, taken from a Monte Carlo Glauber calculation (see appendix A). Here, the open circles and squares represent $\langle p_T \rangle$ for positive and negative hadrons, respectively. The filled symbols show $\langle p_T \rangle$ for charged hadrons evaluated from power-law fits to the $(h^+ + h^-)/2$ transverse momentum distributions. The vertical bars show the statistical and systematic uncertainties. They are rather large as a result of the strong correlation between $\langle p_T \rangle$ and n in the power-law function. For our highest multiplicity class we measure $\langle p_T \rangle = (0.521 \pm 0.011)$ GeV/c for charged hadrons. This represents an increase of about 20% over Pb+Pb collisions at CERN energies at corresponding centralities [20]. Taking the scaled UA1 $p + \bar{p}$ data [1, 21] as a reference, we find $\langle p_T \rangle$ to be increased by about 33% in the top 5% central Au+Au collisions.

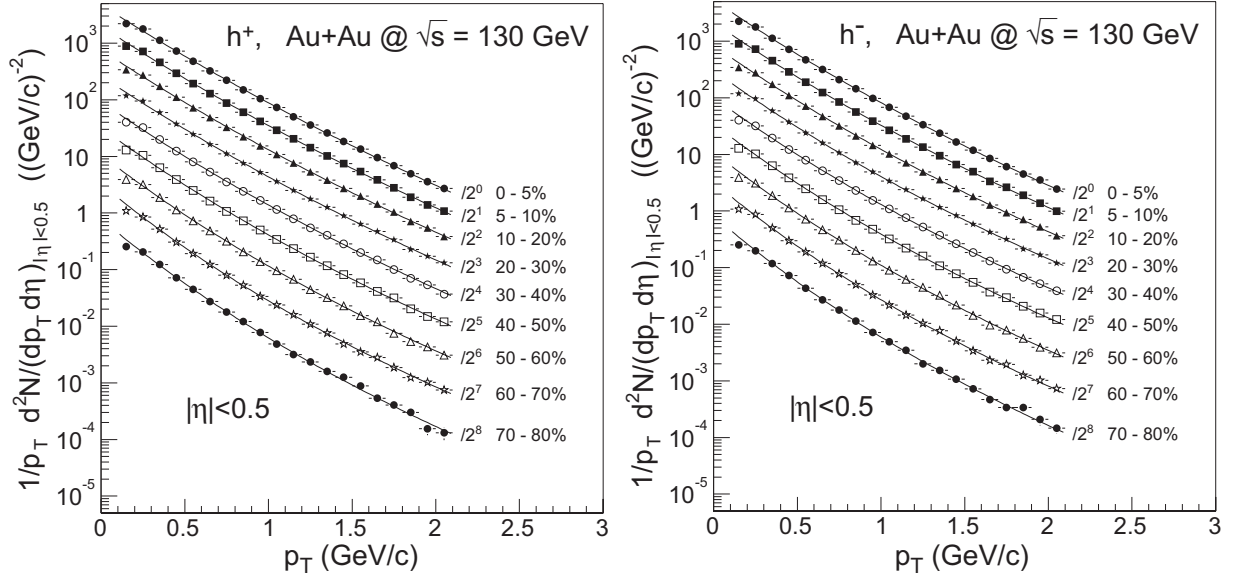


FIG. 6: Positively (left) and negatively (right) charged hadron distributions $(1/p_T) d^2N/(dp_T d\eta)$ for 9 multiplicity classes in the pseudo-rapidity interval $|\eta| < 0.5$. The spectra are scaled by successive powers of 2 as indicated and fit with a power-law function (lines).

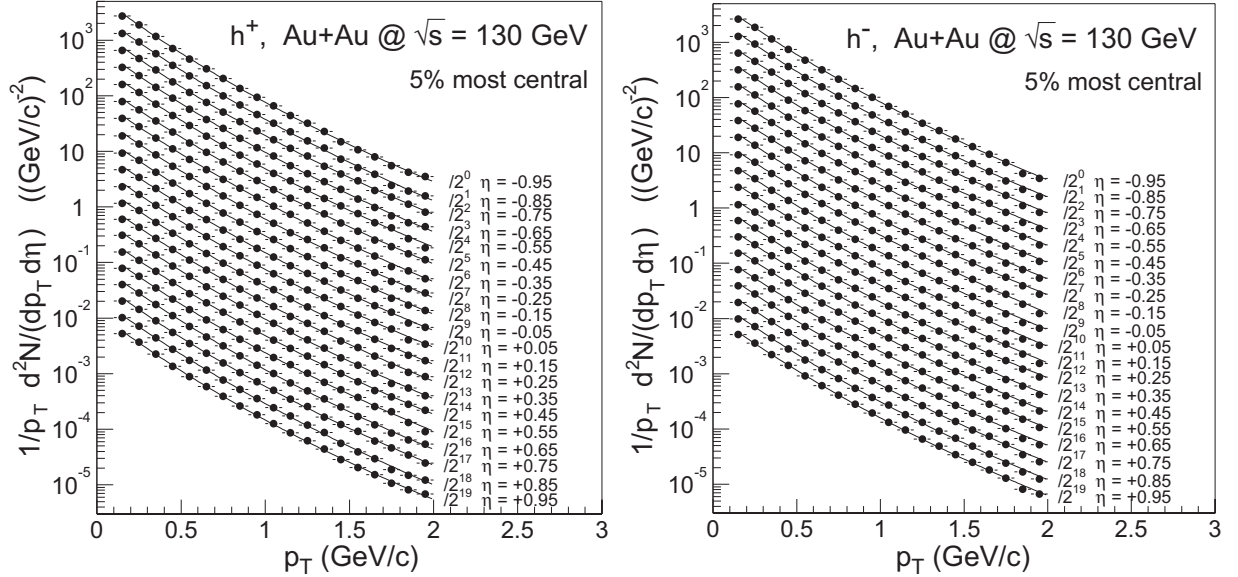


FIG. 7: Positively (left) and negatively (right) charged hadron distributions $(1/p_T) d^2N/(dp_T d\eta)$ of the top 5% central events for 20 different pseudo-rapidity intervals. The spectra are scaled by successive powers of 2 as indicated and fit with a power-law function (lines).

The measured $\langle p_T \rangle$ values for positive and negative hadrons agree within the uncertainties, although the centrality dependence indicates a small gap opening up for

more central events. We attribute this mostly to the ratio $\bar{p}/p \approx 0.7$ [22, 23] and, to some extent, to the ratio $K^-/K^+ \approx 0.9$ [19, 24], since the pion inverse slope

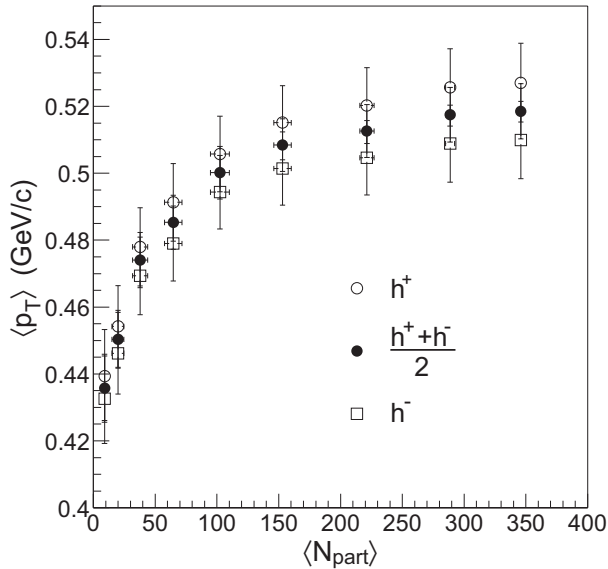


FIG. 8: Charged hadron mean transverse momentum $\langle p_T \rangle$ as a function of average number of participating nucleons $\langle N_{part} \rangle$.

parameter and yields are identical within the uncertainties for all centralities (see below). However, the p and \bar{p} spectra harden significantly with increasing centrality. Hence, the proton and antiproton contributions to the total charged hadrons yield at higher transverse momenta are increasing with N_{part} . This causes an increase in $\langle p_T \rangle$, and the almost constant \bar{p}/p ratio [23] leads to a faster increase of $\langle p_T \rangle$ for positive hadrons than $\langle p_T \rangle$ for negative hadrons.

1. Integrated Hadron Yields as a Function of Centrality and Pseudo-Rapidity

In order to extract the $dN/d\eta$ hadron yields, we integrate the p_T distributions in the region $0.2 < p_T/(\text{GeV}/c) < 2.0$ and use the power-law fits to extrapolate to $p_T = 0$ and $p_T = \infty$. The contribution of extrapolations to the total yields is about 20%. Multiplying these yields by a factor of $2/N_{part}$, we obtain integrated charged hadron densities ($2/N_{part}$) ($dN_{ch}/d\eta$). It has been argued [7] that the centrality dependence of this observable could distinguish between different models of particle production.

Models based on the assumption of a final state gluon saturation advocate a decrease of the charged particle multiplicities per participant nucleon with increasing centrality. A representative of these models is the EKRT model [25], which parameterizes the rapidity density as

$$\left. \frac{dN_{ch}}{d\eta} \right|_{b=0} = C \frac{2}{3} 1.16 A^{0.92} (\sqrt{s})^{0.4}. \quad (3)$$

Following the approach of [26] we generalize Eq. 3 for

non-central collisions by replacing the nuclear mass number A with $N_{part}/2$.

Models based on initial state gluon saturation (e.g. the color glass condensate model [27, 28]) or pQCD inspired models (e.g. the Hijing [16, 17] or the *soft/hard* scattering model used in [26]) predict an increase of the rapidity density with centrality. In both the Hijing and the *soft/hard* model, particle production arises from two major contributions: (a) a *soft* component scaling with the number of participants N_{part} , and (b) a *hard* component from mini-jet production, which is directly proportional to the number of binary collisions N_{bin} and the average inclusive jet cross-section:

$$\frac{dN_{ch}}{d\eta} = n_{soft} \langle N_{part} \rangle + f \langle N_{bin} \rangle \frac{\sigma_{jet}^{AA} A(\sqrt{s})}{\sigma_{in}^{NN}}. \quad (4)$$

Here, n_{soft} gives the amount of charged hadrons produced per soft collision directly, while f describes the linear rise of charged particles produced per hard collision. Reference [26] rewrites Eq. 4 as

$$\frac{dN_{ch}}{d\eta} = (1 - x_{hard}) n_{pp} \frac{\langle N_{part} \rangle}{2} + x_{hard} n_{pp} \langle N_{bin} \rangle \quad (5)$$

and identifies x_{hard} as the fraction of hard collisions. $n_{pp} = 2.25$ is the charged particle pseudo-rapidity density measured from non-single diffractive $p\bar{p}$ interactions and parameterized as $n_{pp} = 2.5 \pm 1.0 - (0.25 \pm 0.19) \ln(s) + (0.023 \pm 0.008) \ln^2(s)$ [29].

In the following, we call Eq. 3 and 5 the EKRT and Kharzeev-Nardi(K/N) parameterizations, respectively, and use them to study the discrimination power of our data against the two opposing models of particle production.

Unfortunately, neither N_{part} nor N_{bin} can be directly measured in the experiment. They can only be derived by calculating the nuclear overlap integral with the help of Glauber calculations and assuming the nucleus-nucleus cross-section. However, two different flavors of Glauber calculations, the optical and the Monte Carlo Glauber calculations, lead to different values for N_{part} and N_{bin} and to rather large uncertainties for peripheral collisions (for details see appendix A).

Figure 9 shows the extracted yields as the pseudo-rapidity density per participant pair ($2/N_{part}$) ($dN/d\eta$) versus the number of participants N_{part} for our centrality classes, where we have calculated N_{part} and N_{bin} using a Monte Carlo Glauber calculation for the right panel, and an optical Glauber calculation for the left panel. In both panels, the vertical bars represent only the uncorrelated statistical uncertainties (including the extrapolation into the not measured p_T regions) folded with the uncertainties on the $\langle N_{part} \rangle$ values. The latter dominate the uncertainties for peripheral collisions and are shown as the horizontal bars. An additional correlated systematic uncertainty of 5% due to acceptance and efficiency corrections has to be taken into account.

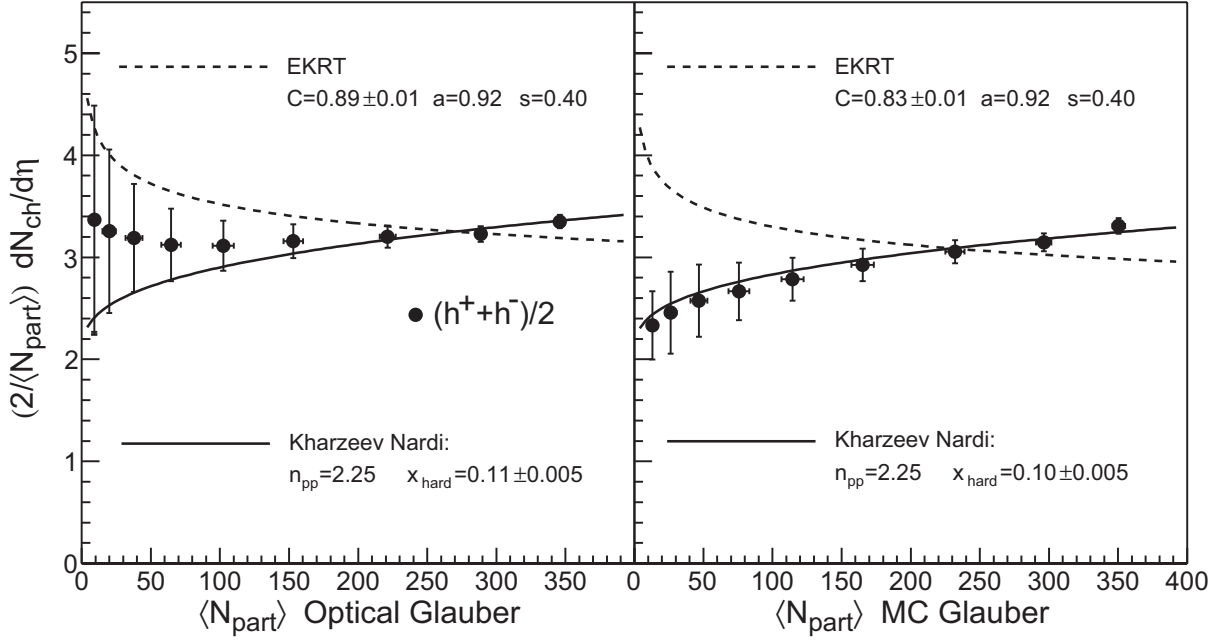


FIG. 9: The rapidity density per participant nucleon pair ($2/\langle N_{part} \rangle$) ($dN_{ch}/d\eta$) versus the number of participants N_{part} . Left: N_{part} was calculated using an optical Glauber calculation. Right: N_{part} was calculated using a Monte Carlo Glauber calculation.

As seen on the left panel of Fig. 9 (using the optical Glauber calculations), we observe no significant change in charged hadron production as a function of centrality in contrast to the EKRT and K/N parameterizations. Furthermore, neither our data nor the EKRT parameterization approach $n_{pp} = 2.25$ in the limit of $N_{part} = 2$. Not surprisingly the final state gluon saturation (EKRT) model breaks down for very peripheral collisions. The K/N parameterization describes our data slightly better and recovers $n_{pp} = 2.25$ for $N_{part} = 2$ due to the fact that it is a built-in parameter of the model.

When using the Monte Carlo Glauber Model to evaluate $\langle N_{part} \rangle$ and $\langle N_{bin} \rangle$ as done in the right panel, our data are consistent with $n_{pp} = 2.25$ in the limit of $N_{part} = 2$, and clearly exhibit a centrality dependence rising from the most peripheral to the most collisions (by about 40%). Fitting Eq. 3 and 5 to the data points, we find the EKRT parameterization clearly failing to describe our data due to the opposite centrality dependence, while the K/N parameterization nicely fits. We evaluate the fraction of hard collisions x_{hard} as 0.10 ± 0.01 for our most central events. The fraction of produced particles originating from hard collisions is then calculated as

$$F_{hard} = \frac{x_{hard} n_{pp} N_{bin}}{dN_{ch}/d\eta} = 0.37 \pm 0.02. \quad (6)$$

Both the values for x_{hard} and F_{hard} agree with the numbers quoted by [2] and [26] although [26] used an optical Glauber model to estimate N_{part} .

It is worth noting that the normalized pseudo-rapidity density ($2/N_{part}$) ($dN/d\eta$) in the EKRT parameterization has only the overall scale C as a free parameter. The centrality dependence is fixed by $A^{a=0.92}$. However, in the K/N parameterization the overall scale is adjusted by $n_{pp} = 2.25$, while the centrality dependence changes with the free parameter x_{hard} . Letting both the overall scale (C/n_{pp}) and the centrality dependence (a/x_{hard}) float freely, both parameterizations describe our data very well with only small changes of the parameters ($\approx 20\%$), independent of which Glauber calculation we use. However, when using the Monte Carlo Glauber calculation and letting the exponent a for the EKRT parameterization float freely, the fit converges at $a = 1.12 \pm 0.03$, thus reversing the centrality dependence from falling to rising with N_{part} .

Summarizing the comparison of our data to the Kharzeev-Nardi and EKRT model, we conclude that due to the uncertainties from the Glauber calculations, we can not explicitly rule out either of the models.

The p_T -integrated yields $dN/d\eta$ as a function of pseudo-rapidity are shown in Fig. 10 for our 9 centrality bins. The vertical bars reflect the uncorrelated statistical uncertainties only. Additional uncertainties from the extrapolation of the power-law fits (2%), from acceptance, reconstruction and trigger efficiency corrections (5%) have to be taken into account. We do not observe any significant difference between positive (open symbols) and negative (closed symbols) hadrons. The

lines fitted to the data points reflect the expectation of a Lorentz-boost invariant source, leading to $dN/d\eta$ distributions suppressed by a factor $(1 - \langle m \rangle^2 / \langle m_T \rangle^2)^{\frac{1}{2}}$ compared to the dN/dy value at mid-rapidity. Our data are in good agreement with this assumption.

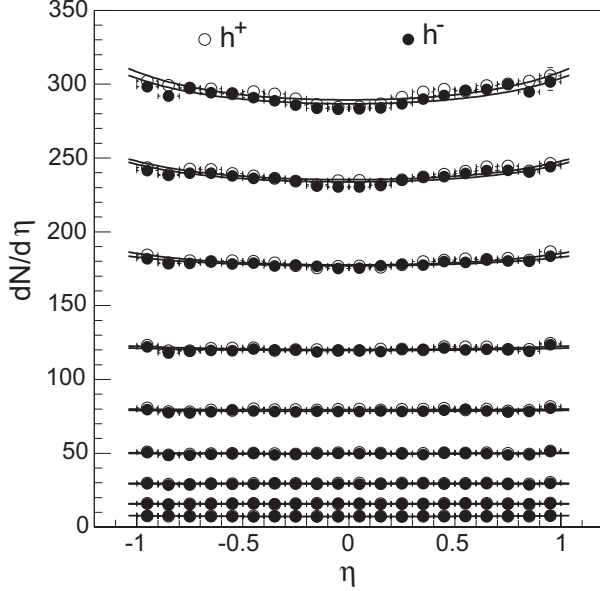


FIG. 10: The charged hadron yields $dN/d\eta$ as a function of pseudo-rapidity for various centralities. The vertical bars reflect the uncorrelated statistical uncertainties.

2. Estimating the Bjorken Energy Density

The Bjorken energy density [8] can be calculated as:

$$\epsilon_{BJ} = \frac{d\langle E_T \rangle}{dy} \frac{1}{F\tau}, \quad (7)$$

where E_T is the transverse energy, τ the formation time and $F = \pi r_0^2 A^{\frac{2}{3}}$. Since we do not measure transverse energy, but only charged particle transverse momenta, we use the approximation

$$\frac{d\langle E_T \rangle}{dy} \approx \langle m_T \rangle \frac{3}{2} \frac{dN_{ch}}{dy}. \quad (8)$$

Here, we used $A = N_{part}/2$ and calculated $\langle m_T \rangle$ from the π^\pm , K^\pm and p, \bar{p} transverse momentum spectra presented in this work, in [19, 24], and in [22, 23], respectively. The factor 3/2 compensates for the neutral particles. Isospin effects estimated to be less than 2% are neglected. Furthermore, following [30] we can substitute

$$\sqrt{1 - m^2 / \langle m_T \rangle^2} \frac{dN}{dy} = \frac{1}{a} \frac{dN}{dy} = \frac{dN}{d\eta} \quad (9)$$

at mid-rapidity and write our estimate of the Bjorken energy density as

$$\epsilon_{BJ} = \frac{3}{2} a \langle m_T \rangle \frac{dN_{ch}}{d\eta} \frac{1}{F\tau}. \quad (10)$$

Plotting the Bjorken energy density as a function of $\langle N_{part} \rangle$ in Fig. 11, we have to take the different $\langle N_{part} \rangle$ values from optical Glauber (open circles) and Monte Carlo Glauber (full circles) into account. For central collisions the differences are negligible and we derive $\epsilon_{BJ} \cdot \tau = 4.2 \pm 0.3$ GeV/fm² for our 5% most central events. The lines in Fig. 11 represent fits to a second order polynomial which is used to evaluate the Bjorken energy density for head on collisions with $N_{part} = 2 \cdot A = 2 \cdot 197$, leading to $\epsilon_{BJ}^A \cdot \tau = 4.4 \pm 0.3$ GeV/fm². Our value is in good agreement with the value $\epsilon_{BJ} \cdot \tau = 4.6$ GeV/fm² quoted in [31] for the most central 2% inelastic collisions (square). At SPS energies, the formation time is traditionally taken

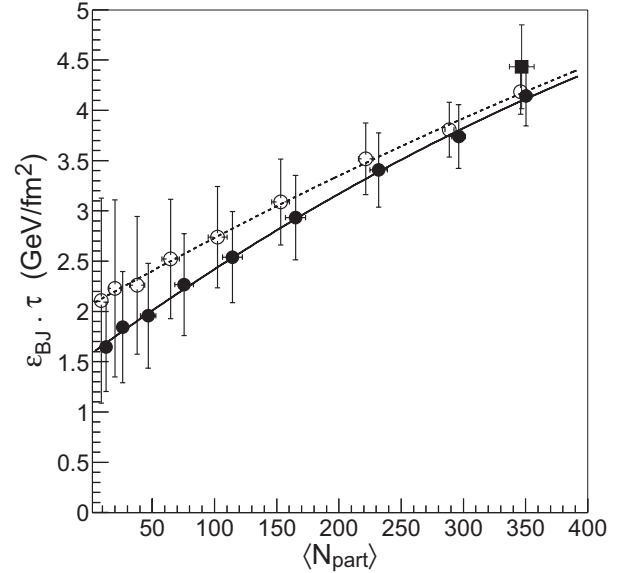


FIG. 11: Estimate of the product of the Bjorken energy density and the formation time ($\epsilon_{BJ} \cdot \tau$) as a function of centrality N_{part} . The open and full circles present the results of this analysis using the optical and Monte Carlo Glauber model, respectively. The square shows the result we have calculated from [31].

as $\tau = 1$ fm resulting in $\epsilon_{BJ} = 3.2$ GeV/fm³ [31, 32] for head-on collisions. At RHIC, the choice of τ is still a matter of debate. While Ref. [33] uses $\tau = 0.6$ fm for their hydrodynamic model ($\sqrt{s_{NN}} = 200$ GeV), Ref. [34] uses $\tau = 0.2$ fm evaluated from the energy loss of high- p_T π^0 in $\sqrt{s_{NN}} = 130$ GeV Au+Au collisions. Applying these values, we obtain $\epsilon_{BJ} = 7.3 \pm 0.5$ GeV/fm³ and $\epsilon_{BJ} = 21.9 \pm 1.6$ GeV/fm³, respectively.

It should be noted that due to final state interactions, measured (final) total transverse energies and energy densities are expected to be less than initial ones [35] and that the Bjorken energy density ϵ_{BJ} as calculated here is not necessarily a thermalized energy density. It cannot directly be compared to, e.g., energy densities calculated on the lattice.

B. Pions

Correcting the recorded pion yields as described in section III, we again obtain the double differential cross-sections $(1/p_T) d^2N/(dp_T dy)$ for π^- and π^+ in 9 centrality and 20 rapidity intervals. Figure 12 presents the mid-rapidity π^- and π^+ spectra as a function of centrality. In both plots the uncorrelated uncertainties are smaller

than the symbols ($< 7\%$). We estimate an additional 5% correlated uncertainty resulting from acceptance, reconstruction and trigger efficiency corrections. We fit Bose-Einstein distributions $(1/p_T) d^2N/(dp_T dy) = A/(\exp(m_T/T) - 1)$ as well as m_T -exponential distributions $(1/p_T) d^2N/(dp_T dy) = A \exp(-m_T/T)$ to our data. The latter are shown as lines in Fig. 12.

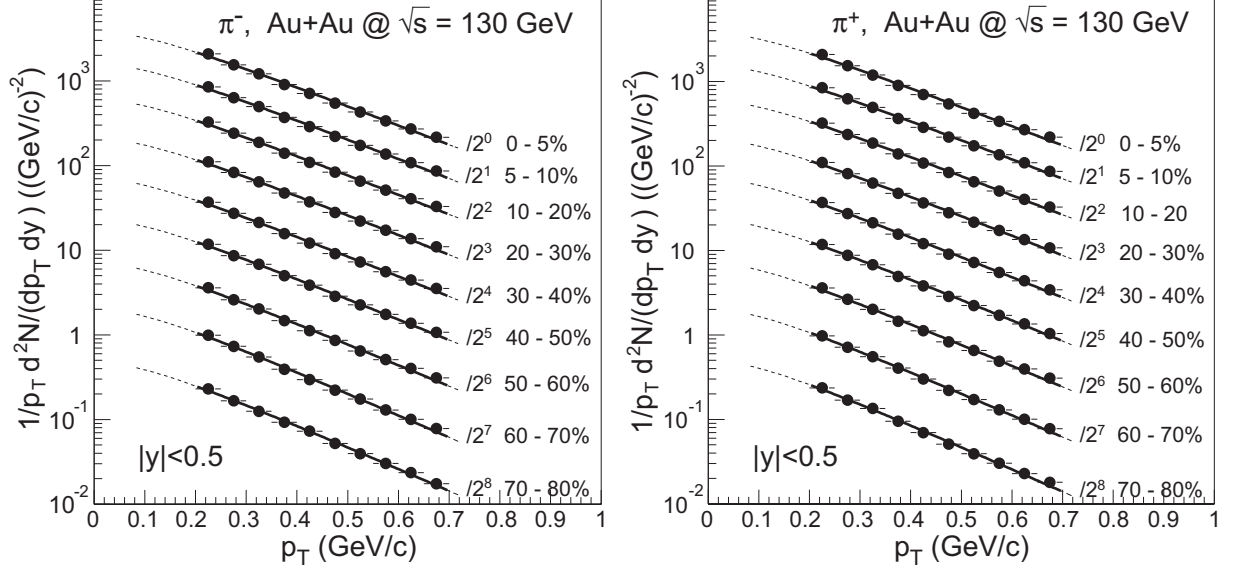


FIG. 12: π^-, π^+ distributions $(1/p_T) d^2N/(dp_T dy)$ at mid-rapidity for 9 different centralities. The spectra are scaled by successive powers of 2 as indicated. The numbers to the right give the fraction of the hadronic cross section of the centrality class.

For the most central events, we extract an inverse slope parameter $T_{exp} = 187 \pm 1(stat) \pm 8(fit)$ MeV for positive and negative pions, compatible with the value $T = 187 \pm 6$ MeV for π^- and $T = 193 \pm 3$ MeV for π^+ reported by [36] for Pb+Pb collisions at $\sqrt{s_{NN}} = 17.2$ GeV of similar centrality, using an exponential distribution in a similar p_T range. However, while the uncertainties on the fit parameters resulting from statistics (*stat*) and the actual fit procedure (*fit*) are only on the order of 5% percent, using a Bose-Einstein distribution as the fit function will lead to a $\approx 15\%$ increase in the extracted inverse slope parameter: $T_{BE} = 218 \pm 2(stat) \pm 8(fit)$. As for the extracted integrated yields dN/dy , the difference resulting from the choice of the fit functions is about 7%, with $dN/dy_{exp} = 229 \pm 3(stat) \pm 3(fit)$ and

$$dN/dy_{BE} = 249 \pm 3(stat) \pm 2(fit) .$$

The reason for choosing the m_T -exponential and Bose-Einstein distributions as fit functions lies in their different low- p_T behavior, the first bending downwards, the latter bending upwards as compared to a straight p_T -exponential in the representation $(1/p_T) d^2N/(dp_T dy)$. We conclude that the differences between our results evaluated with the two fit functions present good estimates of the systematic uncertainties and lead to averaged values of $dN/dy = 239 \pm 3(stat) \pm 2(fit) \pm 10(sys)$ and $\langle p_T \rangle = 405 \pm 3(stat) \pm 2(fit) \pm 7(sys)$ MeV/c for our most central collisions for positive and negative pions.

Changing the fit range or function does not significantly affect the centrality dependence of the pion yields, inverse slopes T , or $\langle p_T \rangle$ as shown in Fig. 13.

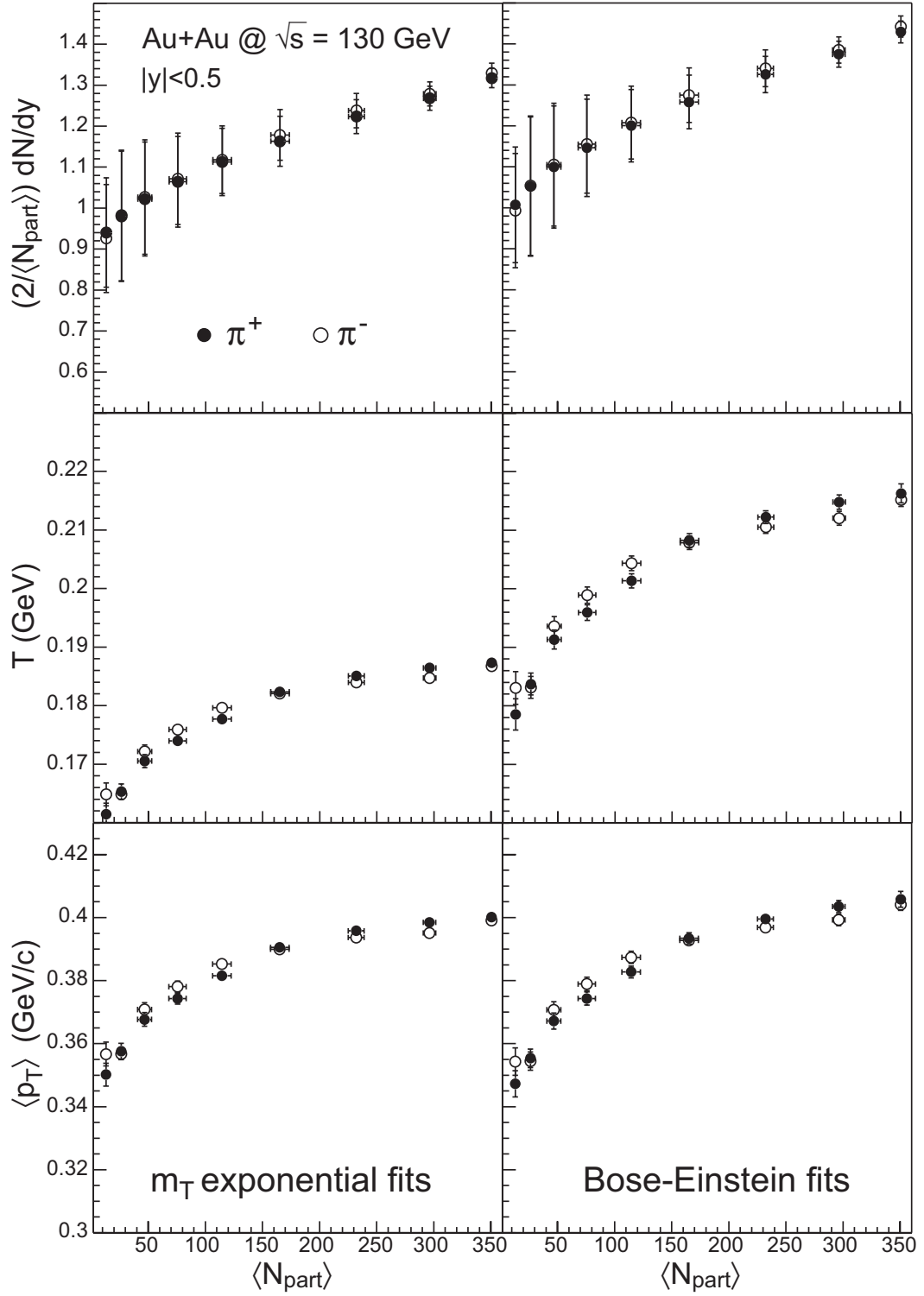


FIG. 13: Top: Integrated π^\pm yields per participant pair $2/\langle N_{part} \rangle dN/dy$ as a function of centrality. Middle: The extracted inverse slope parameters T as a function of centrality. Bottom: $\langle p_T \rangle$ as a function of centrality. Closed symbols: π^+ , open symbols: π^- . Left: Using an m_T -exponential fit function. Right: Using a Bose-Einstein fit function. All panels present data from the mid-rapidity region $|y| < 0.5$ only. The vertical bars represent the uncorrelated statistical uncertainties only. The horizontal bars reflect the uncertainties on the $\langle N_{part} \rangle$ values. Systematic uncertainties are discussed in the text.

The two columns present the results when using the m_T -exponential (left) and Bose-Einstein (right) fits. The top row shows the rapidity density $(2/N_{part}) (dN/dy)$ against the number of participating nucleons $\langle N_{part} \rangle$, taken from the Monte Carlo Glauber calculation. We find the normalized yields to increase by about 40% between our most peripheral and most central collisions. The inverse slope parameters T (middle) and $\langle p_T \rangle$ values (bottom) increase by roughly 15%. We do not observe any significant differences between π^- and π^+ production. This similarity between π^- and π^+ is also reflected in the pion spectra themselves. The π^-/π^+ ratio is consistent with unity over the measured transverse momentum range. In this, our pion results differ qualitatively from the observed π^- over π^+ excess at low transverse momenta in central Pb+Pb collisions at $\sqrt{s_{NN}} = 17$ GeV reported in Ref. [37]. There the authors attribute this excess to Coulomb interactions and the large amount of net charge in the system. Our finding $\pi^-/\pi^+ = 1.00 \pm 0.02$ does not contradict their results and is expected in the light of an almost net-baryon free and isospin symmetric mid-rapidity region at RHIC.

Taking the differences between $dN/d\eta$ and dN/dy into account, we conclude that pions constitute about $(82 \pm 5)\%$ of the charged hadrons for the most central events,

and about $(90 \pm 5)\%$ for peripheral events (60-80% of the hadronic cross section) at mid-rapidity.

Figure 14 presents the rapidity dependence of our pion spectra for the top 5% central collisions. The reason for the varying fit ranges is the total momentum limit $p < 0.7$ GeV/c for pion identification, which translates to the indicated p_T values as a function of rapidity. Again, only the statistical uncertainties are shown and the lines present the m_T -exponential fits.

The extracted yield dN/dy and inverse slope parameter T as a function of rapidity are shown in Fig. 15 for four and three centrality classes, respectively. The shaded bands in all four panels represent the uncorrelated systematic uncertainties for the 0-5% most central events. The uncorrelated systematic uncertainties for the other centrality classes are of the same relative size. We do not observe any significant change of the integrated yields dN/dy (top) within our rapidity coverage. The extracted inverse slope parameters T (bottom) seem to decrease for $|y| > 0.5$. However, since the uncorrelated systematic and statistical uncertainties increase for larger rapidities, we can not conclusively rule out a boost-invariant source extending beyond $|y| = 0.5$. Within our uncertainties we do not find a change in the shape of the $dN/dy(y)$ and $T(y)$ distributions with centrality.

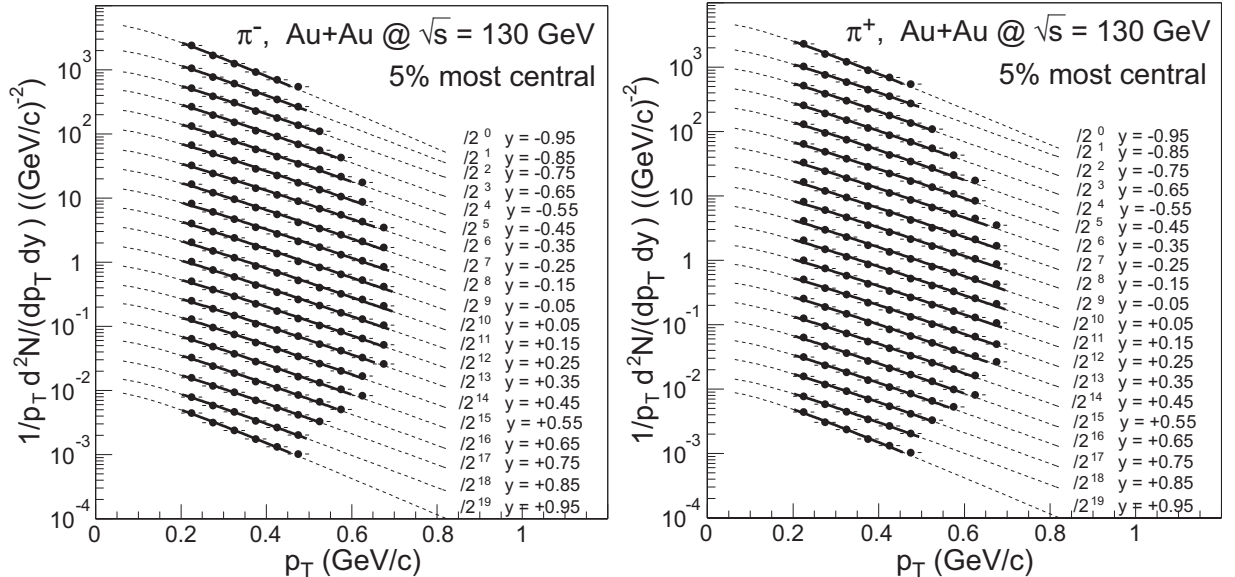


FIG. 14: π^-, π^+ distributions $(1/p_T) d^2N/(dp_T dy)$ of the top 5% central events for 20 different rapidity intervals. The spectra are scaled by successive powers of 2 as indicated.

V. SUMMARY

In summary, we have measured the transverse momentum distributions of charged hadrons and pions as a func-

tion of centrality and (pseudo-)rapidity in Au+Au collisions at $\sqrt{s_{NN}} = 130$ GeV.

For our most central event sample (top 5%), we mea-

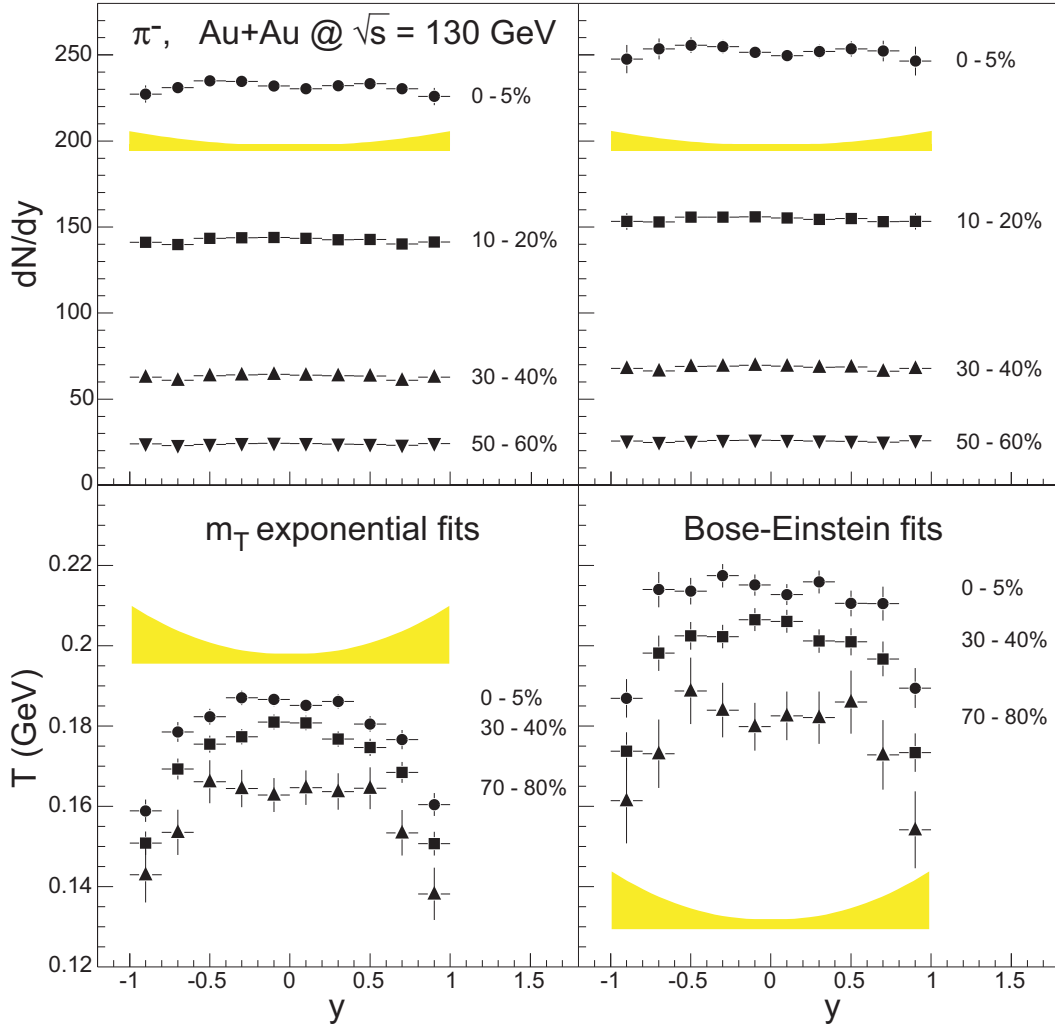


FIG. 15: Top: Integrated π^- yield dN/dy as a function of rapidity. Bottom: Inverse slope parameter T as a function of rapidity. Left: Using an m_T -exponential fit function. Right: Using a Bose-Einstein fit-function. The vertical bars represent the uncorrelated statistical uncertainties. The shaded bands show the uncorrelated systematic uncertainties for the 0-5% centrality class.

sure the charged hadron mean transverse momentum $\langle p_T \rangle$ to be 0.52 GeV/c, about 33% higher than in $p\bar{p}$ at the same energy. $\langle p_T \rangle$ decreases gradually for more peripheral events and seems to recover the $p\bar{p}$ value of 0.392 GeV/c in the limit of $N_{part} = 2$. Compared to Pb+Pb collisions of similar centrality at $\sqrt{s_{NN}} = 17.2$ GeV (SPS), we find an increase of $\langle p_T \rangle$ of about 20%.

Although final stage gluon saturation models (i.e. the EKRT model) and two component (*soft/hard*) models predict qualitatively different behavior for the mid-rapidity particle production per participating nucleon pair ($2/N_{part}$) (dN/dy) as a function of centrality, we conclude that uncertainties in the determination of N_{part} do not permit to rule out either model.

Estimating the Bjorken energy density, we find $\epsilon_{BJ} = 4.2 \pm 0.3$ GeV/fm³ in central collisions when making the conservative assumption of the formation time τ being

1 fm at RHIC.

For the mid-rapidity pion production, we measure an increase of roughly 40% for the normalized π^+ and π^- rapidity density ($2/N_{part}$) (dN/dy) from the most peripheral to the most central collisions, leading to $dN^{\pi^\pm}/dy = 239 \pm 3(stat) \pm 2(fit) \pm 10(sys)$ for the top 5% central collisions. The corresponding inverse slope parameters T and $\langle p_T \rangle$ values increase by about 15%.

The rapidity dependence of the pion yields $dN/dy(y)$ and inverse slope parameters $T(y)$ is in agreement with a Lorentz-boost invariant source of at least one unit of rapidity around mid-rapidity ($|y| < 0.5$).

APPENDIX A: THE GLAUBER MODEL

In recent theoretical publications [26, 38, 39, 40, 41], the production of hadrons in heavy ion collisions at RHIC

has been parameterized as a function of the number of participating nucleons N_{part} and the number of binary collisions N_{bin} . Neither N_{part} nor N_{bin} can be measured directly in the experiment. Their values can only be derived by mapping the measured data, i.e. the dN/dN_{ch} distributions, to the corresponding distribution obtained from phenomenological calculations, thus relating N_{part} and N_{bin} to the measured dN/dN_{ch} distributions. These types of calculations are generally called Glauber calculations and come in two flavors, the *optical* and the *Monte-Carlo* Glauber calculations.

The optical model is based on an analytic consideration of classically overlapping nuclei [26, 30, 42, 43]. The Monte Carlo approach is based on a computer simulation of billiard ball like colliding nucleons [18, 44, 45, 46, 47].

However, as already noted in Ref. [48], different implementations of the Glauber model, such as the one used in the frequently quoted Kharzeev/Nardi *soft+hard* collision parameterization [26] (optical) or in the popular Hijing model (Monte Carlo) [16], lead to slightly different values for N_{part} and N_{bin} , especially for peripheral collisions. Therefore, any results reported in terms of Glauber quantities must be carefully interpreted based upon specifics of the underlying calculations.

In the following we will briefly report on the Glauber calculations performed to obtain the N_{bin} and N_{part} values used in this manuscript. Tables II and III present the mapping of $\langle N_{part} \rangle$ and $\langle N_{bin} \rangle$ values obtained from the optical and Monte Carlo Glauber calculations to our multiplicity classes, respectively.

a. The Optical Glauber Model

For our optical Glauber calculation, we start by assuming a spherically symmetric Woods-Saxon density profile

$$\rho(r) = \frac{\rho_0}{1 + \exp(\frac{r-r_0}{c})} \quad (\text{A1})$$

with the parameters $\rho_0 = 0.169/\text{fm}^3$ and $c = 0.535 \pm 0.027$ fm, as reported for Au nuclei in [49]. From the same publication we extracted the value for r_0 , but increased its value from 6.38 fm to 6.5 ± 0.1 fm to approximate the effect of the neutron skin. By integrating equation A1, we obtain $N_{Au}^{Au} = \int dr \rho(r) 4\pi r^2 = 196.6$ and renormalized ρ_0 so that we obtain 197 as the correct total number of nucleons from the integral. $\rho_0(r)/N_{Au}^{Au}$ is interpreted as the probability to find a nucleon in the volume element $d^3x = d^2b dz$ at (\vec{b}, z) . The nuclear overlap integral $T_{AA}(b) = \int d^2s dz_1 dz_2 \rho_1(\vec{s}, z_1) \rho_2(\vec{s} - \vec{b}, z_2)$ can now be calculated as the integral over two density profiles, where \vec{b} is the impact parameter, \vec{s} a vector perpendicular to the beam-axis z , and z_1 and z_2 coordinates along z . Integrated over the whole impact parameter range and normalized to unity $\int d^2 T_{AA}(\vec{b}) = 1$, we now define the probability to have n interactions at a given

impact parameter as

$$P(n, b) = \binom{A^2}{n} (T_{AA}(b) \sigma_{pp})^n (1 - T_{AA}(b) \sigma_{pp})^{A^2 - n} \quad (\text{A2})$$

Here, we assume that the interaction probability is solely given by the proton-proton cross-section $\sigma_{pp} = 41 \pm 1$ mb, thus neglecting effects like excitation and energy loss. Furthermore, assuming that the proton-proton and the proton-antiproton cross-sections are almost identical at energies above $\sqrt{s_{NN}} = 100$ GeV as indicated in [50], and using the parameterizations of the proton-antiproton total and inelastic cross-sections as a function of energy therein, we determine the total hadronic cross-section for Au+Au collisions at $\sqrt{s_{NN}} = 130$ GeV as

$$\sigma_{AuAu} = \int d^2b \left[1 - (1 - T_{AA}(b) \sigma_{pp})^{A^2} \right] = 6.9 \text{ barn} \quad (\text{A3})$$

The number of binary collisions N_{bin} and the number of participants N_{part} for a given impact parameter are derived from T_{AA} as

$$N_{bin}(b) = \sigma_{pp} A A T_{AA}(b) \quad (\text{A4})$$

$$N_{part}(b) = 2A \int d^2s T_{AA}(\vec{s}) \quad (\text{A5})$$

$$\left\{ 1 - \left(1 - T_{AA}(\vec{s} - \vec{b}) \sigma_{pp} \right)^{A^2} \right\} \quad (\text{A6})$$

To relate N_{part} and N_{bin} to the experimental observable $\langle N_{ch} \rangle$, the mean of the total number of charged tracks in our multiplicity classes, we use Eqs. A3, A4 and A5 to generate the functions $d\sigma/dN_{bin}$ and $d\sigma/dN_{part}$. Mathematically, one must account for the Jacobian in these transformations, which is cumbersome. It is more convenient to use Monte Carlo techniques to calculate $d\sigma/dN_{bin}$ and $d\sigma/dN_{part}$, where the Jacobian is intrinsic to the method. Therefore, we randomly sample the differential cross-section $d\sigma/db$ of equation A3 and histogram the values of N_{bin} and N_{part} for each sampling. We then obtain the distributions $d\sigma/dN_{bin}$ and $d\sigma/dN_{part}$. Each distribution was divided into bins corresponding to common fractions of the total cross-section. The mean values of the bins were then correlated with the independently measured mean values of, e.g., N_{ch} . Potential biases due to this bin-by-bin evaluation of mean values were investigated and found to be negligible in comparison to the other sources of systematic uncertainties. This method was chosen instead of the example given in [26], which relies upon a specific model of particle production. The uncertainties on the values given in Table II were evaluated by varying the total hadronic cross-section σ_{AuAu} by $\pm 5\%$ and the input parameters σ_{pp} , c and r_0 within their uncertainties.

bin#	0	1	2	3	4	5	6	7	8	9	10
$\sigma/\sigma_{tot}(\%)$	100 - 0	100 - 80	80 - 70	70 - 60	60 - 50	50 - 40	40 - 30	30 - 20	20 - 10	10 - 5	5 - 0
$\langle N_{part} \rangle$	93.0 ^{+3.8} _{-0.9}	2.2 ^{+1.1} _{-0.7}	9.0 ^{+2.9} _{-3.3}	19.9 ^{+4.6} _{-5.6}	37.7 ^{+6.5} _{-7.0}	64.1 ^{+9.5} _{-8.1}	101.4 ^{+10.6} _{-8.1}	152.6 ^{+8.6} _{-9.0}	220.9 ^{+7.0} _{-8.7}	287.7 ^{+5.5} _{-6.2}	345.2 ^{+2.8} _{-3.5}
$\langle N_{bin} \rangle$	220.6 ^{+24.9} _{-14.1}	1.7 ^{+1.1} _{-0.7}	8.3 ^{+3.3} _{-3.7}	21.8 ^{+8.9} _{-7.6}	50.8 ^{+16.8} _{-13.5}	105.5 ^{+24.8} _{-22.5}	196.7 ^{+36.8} _{-31.5}	341.4 ^{+47.7} _{-43.5}	562.1 ^{+59.1} _{-55.6}	799.8 ^{+67.1} _{-61.5}	1024.2 ^{+72.1} _{-69.4}
$\langle b \rangle / \text{fm}$	9.2 ^{+0.3} _{-0.2}	14.4 ^{+0.7} _{-0.6}	13.1 ^{+0.6} _{-0.7}	12.2 ^{+0.5} _{-0.7}	11.2 ^{+0.5} _{-0.6}	10.2 ^{+0.5} _{-0.5}	9.0 ^{+0.5} _{-0.4}	7.6 ^{+0.4} _{-0.4}	5.8 ^{+0.3} _{-0.3}	4.1 ^{+0.2} _{-0.2}	2.4 ^{+0.1} _{-0.1}
$\langle \frac{N_{bin}}{N_{part}} \rangle$	1.6 ^{+0.1} _{-0.1}	0.7 ^{+0.1} _{-0.0}	0.9 ^{+0.1} _{-0.1}	1.1 ^{+0.1} _{-0.1}	1.3 ^{+0.2} _{-0.1}	1.6 ^{+0.2} _{-0.1}	1.9 ^{+0.2} _{-0.2}	2.2 ^{+0.2} _{-0.2}	2.5 ^{+0.2} _{-0.2}	2.8 ^{+0.2} _{-0.2}	3.0 ^{+0.2} _{-0.2}

TABLE II: Mapping of the multiplicity classes to the optical Glauber calculations.

bin#	0	1	2	3	4	5	6	7	8	9	10
$\sigma/\sigma_{tot}(\%)$	100 - 0	100 - 80	80 - 70	70 - 60	60 - 50	50 - 40	40 - 30	30 - 20	20 - 10	10 - 5	5 - 0
$\langle N_{part} \rangle$	101.6 ^{+1.3} _{-1.2}	4.5 ^{+1.0} _{-1.7}	14.0 ^{+4.0} _{-5.2}	26.9 ^{+6.6} _{-5.5}	47.3 ^{+8.1} _{-7.5}	76.2 ^{+9.0} _{-9.1}	114.5 ^{+10.7} _{-8.6}	165.7 ^{+10.0} _{-8.3}	233.6 ^{+7.4} _{-8.4}	298.3 ^{+5.2} _{-7.1}	351.5 ^{+3.4} _{-3.8}
$\langle N_{bin} \rangle$	229.5 ^{+14.9} _{-14.5}	3.1 ^{+0.9} _{-1.3}	12.3 ^{+4.8} _{-5.1}	29.1 ^{+9.6} _{-8.6}	62.4 ^{+16.3} _{-15.7}	120.6 ^{+25.1} _{-24.5}	214.3 ^{+36.2} _{-33.2}	358.4 ^{+46.3} _{-43.6}	575.8 ^{+54.5} _{-58.1}	804.6 ^{+65.4} _{-64.0}	1020.3 ^{+73.2} _{-68.0}
$\langle b \rangle / \text{fm}$	10.0 ^{+0.5} _{-0.2}	14.4 ^{+0.9} _{-0.5}	12.9 ^{+0.6} _{-0.6}	12.0 ^{+0.5} _{-0.6}	11.1 ^{+0.5} _{-0.5}	10.0 ^{+0.5} _{-0.4}	8.8 ^{+0.4} _{-0.4}	7.5 ^{+0.3} _{-0.3}	5.8 ^{+0.3} _{-0.2}	4.1 ^{+0.2} _{-0.2}	2.2 ^{+0.2} _{-0.1}
$\langle \frac{N_{bin}}{N_{part}} \rangle$	1.5 ^{+0.1} _{-0.1}	0.6 ^{+0.0} _{-0.0}	0.9 ^{+0.1} _{-0.1}	1.1 ^{+0.1} _{-0.1}	1.3 ^{+0.1} _{-0.1}	1.6 ^{+0.1} _{-0.1}	1.9 ^{+0.1} _{-0.1}	2.2 ^{+0.1} _{-0.1}	2.5 ^{+0.2} _{-0.2}	2.7 ^{+0.2} _{-0.2}	3.0 ^{+0.2} _{-0.2}

TABLE III: Mapping of the multiplicity classes to the Monte-Carlo Glauber calculations.

b. The Monte CarloGlauber Model

The Monte Carlo method consists of constructing a set of independently simulated Au+Au interactions. For each interaction, A target nucleons are distributed about the point (0,0,0) and A projectile nucleons are distributed about the point (b ,0,0), where b is the impact parameter of the event. Each of the nucleons is randomly distributed using the Woods-Saxon distribution from equation A1 as the probability profile. The value of ρ_0 is fixed via the normalization

$$197 = \int_0^{+\infty} d^3 r \rho(r) . \quad (\text{A7})$$

We further require that all nucleons in either nucleus be separated by a distance $d \geq d_{min}$ where $d_{min} = 0.4$ fm is characteristic of the length of the repulsive nucleon-nucleon force. With these parameters we find a total cross-section of 6.9 barns. Next, all possible nucleon-nucleon pairs (with one nucleon each from the target and projectile) are constructed. Each pair is determined to 'interact' if they are separated by the transverse distance

$$r \leq \sqrt{\frac{\sigma_{pp}}{\pi}} . \quad (\text{A8})$$

N_{part} is defined as the total number of nucleons that underwent at least one interaction. N_{bin} is defined as the

total number of interactions in the event. This process is iterated for an arbitrary number of events, with the impact parameter b for each event randomly chosen from a flat distribution. Thus, the distributions $d\sigma/dN_{bin}$, $d\sigma/dN_{part}$, and $d\sigma/db$ are determined. Each distribution was divided into bins corresponding to common fractions of the total cross-section, and mean values were extracted on a bin-by-bin basis. These mean values were then correlated with the independently measured mean values of, e.g., N_{ch} . Potential biases due to this bin-by-bin evaluation of mean values were investigated and found to be negligible in comparison to the other sources of systematic uncertainties.

The systematic uncertainties on N_{bin} and N_{part} were determined by varying the Woods-Saxon parameters, by varying the value of σ_{pp} , and by including a 5% uncertainty in the determination of the total measured Au+Au cross-section. The contributions from these three sources were determined separately and were treated as fully correlated in the final systematic uncertainties reported.

Uncertainties due to differences in the mass-density distribution (neutrons) with respect to the measured charge-density distribution (protons) are beyond the scope of this study.

ACKNOWLEDGMENTS

We thank the RHIC Operations Group and RCF at BNL, and the NERSC Center at LBNL for their sup-

port. This work was supported in part by the HENP Divisions of the Office of Science of the U.S. DOE; the U.S. NSF; the BMBF of Germany; IN2P3, RA, RPL,

and EMN of France; EPSRC of the United Kingdom; FAPESP of Brazil; the Russian Ministry of Science and Technology; the Ministry of Education and the NNSFC

of China; SFOM of the Czech Republic, DAE, DST, and CSIR of the Government of India; the Swiss NSF.

-
- [1] C. Adler et al. (STAR), Phys. Rev. Lett. **87**, 112303 (2001), nucl-ex/0106004.
- [2] B. B. Back et al. (PHOBOS), Phys. Rev. **C65**, 061901 (2002), nucl-ex/0201005.
- [3] B. B. Back et al. (PHOBOS), Phys. Rev. Lett. **85**, 3100 (2000), hep-ex/0007036.
- [4] B. B. Back et al. (PHOBOS), Phys. Rev. Lett. **87**, 102303 (2001), nucl-ex/0106006.
- [5] K. Adcox et al. (PHENIX), Phys. Rev. Lett. **86**, 3500 (2001), nucl-ex/0012008.
- [6] K. Adcox et al. (PHENIX), Phys. Rev. Lett. **87**, 052301 (2001), nucl-ex/0104015.
- [7] X.-N. Wang and M. Gyulassy, Phys. Rev. Lett. **86**, 3496 (2001), nucl-th/0008014.
- [8] J. D. Bjorken, Phys. Rev. D **27**, 140 (1983).
- [9] K. H. Ackermann et al. (STAR), Nucl. Phys. **A661**, 681 (1999).
- [10] K. H. Ackermann et al. (STAR), Nucl. Instrum. Meth. **A499**, 624 (2003).
- [11] C. Adler et al., Nucl. Instrum. Meth. **A470**, 488 (2001), nucl-ex/0008005.
- [12] F. S. Bieser et al., Nucl. Instrum. Meth. **A499**, 766 (2003).
- [13] M. Anderson et al., Nucl. Instrum. Meth. **A499**, 659 (2003).
- [14] R. Frühwirth, Nucl. Instrum. Meth. **A262**, 444 (1987).
- [15] D. Liko, STAR Notes **87** (1992), www.star.bnl.gov/star/starlib/doc/www/sno/ice/sn0087.htm
- [16] X. N. Wang and M. Gyulassy, Phys. Rev. D **44**, 3501 (1991).
- [17] X. N. Wang and M. Gyulassy, Comput. Phys. Commun. **83**, 307 (1994), nucl-th/9502021.
- [18] C. Adler et al., Phys. Rev. Lett. **89**, 202301 (2002), nucl-ex/0206011.
- [19] J. Adams et al. (STAR), Phys. Lett. **B567**, 167 (2003).
- [20] H. Appelshäuser et al. (NA49), Phys. Rev. Lett. **82**, 2471 (1999), nucl-ex/9810014.
- [21] C. Albajar et al. (UA1), Nucl. Phys. **B335**, 261 (1990).
- [22] C. Adler et al. (STAR), Phys. Rev. Lett. **87**, 262302 (2001), nucl-ex/0110009.
- [23] C. Adler et al. (STAR), Phys. Rev. Lett. **86**, 4778 (2001), nucl-ex/0104022.
- [24] C. Adler et al. (STAR) (2002), nucl-ex/0206008.
- [25] K. J. Eskola, K. Kajantie, P. V. Ruuskanen, and K. Tuominen, Nucl. Phys. **B570**, 379 (2000), hep-ph/9909456.
- [26] D. Kharzeev and M. Nardi, Phys. Lett. **B507**, 121 (2001), nucl-th/0012025.
- [27] L. McLerran, Nucl. Phys. **A702**, 49 (2002).
- [28] L. McLerran, Nucl. Phys. **A699**, 73 (2002).
- [29] F. Abe et al., Phys. Rev. D **41**, 2330 (1990).
- [30] C.-Y. Wong, *Introduction to High-Energy Heavy-Ion Collisions* (World Scientific, Singapore, 1994).
- [31] K. Adcox et al. (PHENIX), Phys. Rev. Lett. **88**, 192302 (2002), nucl-ex/0201008.
- [32] T. Alber et al. (NA49), Phys. Rev. Lett. **75**, 3814 (1995).
- [33] S. A. Bass and A. Dumitru, Phys. Rev. **C61**, 064909 (2000), nucl-th/0001033.
- [34] E. Wang and X.-N. Wang, Phys. Rev. Lett. **89**, 162301 (2002), hep-ph/0202105.
- [35] K. J. Eskola, P. V. Ruuskanen, S. S. Rasanen, and K. Tuominen, Nucl. Phys. **A696**, 715 (2001), hep-ph/0104010.
- [36] P. G. Jones et al. (NA49), Nucl. Phys. **A610**, 188c (1996).
- [37] H. Boggild et al. (NA44), Phys. Lett. **B372**, 339 (1996).
- [38] D. Kharzeev, E. Levin, and L. McLerran, Phys. Lett. **B561**, 93 (2003), hep-ph/0210332.
- [39] V. Topor Pop et al. (2002), nucl-th/0209089.
- [40] J. Schaffner-Bielich, D. Kharzeev, L. D. McLerran, and R. Venugopalan, Nucl. Phys. **A705**, 494 (2002), nucl-th/0108048.
- [41] S.-Y. Li and X.-N. Wang, Phys. Lett. **B527**, 85 (2002), nucl-th/0110075.
- [42] A. J. Baltz, C. Chasman, and S. N. White, Nucl. Instr. Meth. **A417**, 1 (1998), nucl-ex/9801002.
- [43] F. Antinori et al. (WA97), Nucl. Phys. **A661**, 357 (1999).
- [44] K. Adcox et al. (PHENIX), Phys. Lett. **B561**, 82 (2003), nucl-ex/0207009.
- [45] I. G. Bearden et al. (BRAHMS), Phys. Lett. **B523**, 227 (2001), nucl-ex/0108016.
- [46] B. B. Back et al. (PHOBOS) (2003), nucl-ex/0302015.
- [47] B. B. Back et al. (PHOBOS) (2003), nucl-ex/0301017.
- [48] B. B. Back et al. (PHOBOS), Phys. Rev. **C65**, 031901 (2002), nucl-ex/0105011.
- [49] C. W. deJager, H. deVries, and C. deVries, Atomic Data and Nuclear Data Tables **14**, 485 (1974).
- [50] K. Hagiwara et al. (Particle Data Group), Phys. Rev. **D66**, 010001 (2002).
- [51] As event generators we used complex programs such as the Hijing, RQMD or VINI codes, trying to describe heavy ions collisions as close as possible, as well as simple phase-space generators, distributing a single particle species according to a given phase-space distribution.
- [52] Fragments of a single track that is broken into pieces by the reconstruction software and misidentified as multiple tracks are called *split tracks*. Two or more tracks that are very close in coordinate space might be reconstructed as a single track. These tracks are referred to as *merged tracks*. Tracks that are made up by the reconstruction software and are not associated to a real track (i.e. from random noise in the detector) are called *ghost tracks*.